

Bendable Silicene Membranes

Christian Martella,* Chiara Massetti, Daya Sagar Dhungana, Emiliano Bonera, Carlo Grazianetti, and Alessandro Molle*

Due to their superior mechanical properties, 2D materials have gained interest as active layers in flexible devices co-integrating electronic, photonic, and straintronic functions altogether. To this end, 2D bendable membranes compatible with the technological process standards and endowed with large-scale uniformity are highly desired. Here, it is reported on the realization of bendable membranes based on silicene layers (the 2D form of silicon) by means of a process in which the layers are fully detached from the native substrate and transferred onto arbitrary flexible substrates. The application of macroscopic mechanical deformations induces a strain-responsive behavior in the Raman spectrum of silicene. It is also shown that the membranes under elastic tension relaxation are prone to form microscale wrinkles displaying a local generation of strain in the silicene layer consistent with that observed under macroscopic mechanical deformation. Optothermal Raman spectroscopy measurements reveal a curvature-dependent heat dispersion in silicene wrinkles. Finally, as compelling evidence of the technological potential of the silicene membranes, it is demonstrated that they can be readily introduced into a lithographic process flow resulting in the definition of flexible device-ready architectures, a piezoresistor, and thus paving the way to a viable advance in a fully silicon-compatible technology framework.

in a network of interacting devices envisaging the so-called Internet of Things. In this scenario, bendable membranes will be the building block for applications such as strain sensors, wearable electronics, and photonics, flexible plasmonics, implantable robotic skin, etc.^[2–5] A number of organic and inorganic materials have been mooted as candidates for flexible device integration, and 2D materials may play a key role in this respect as they offer robust mechanical properties, sustaining a high level of strain before fracturing, complemented by optical and electronic properties suitable for application in nano-photonics and -electronics.^[6,7] Moreover, strain engineering has been shown to provide a great opportunity for 2D material-based functional applications taking advantage of mechanisms like electronic bandgap tuning,^[8,9] exciton manipulation,^[10,11] carrier mobility boosting^[12–14] and piezoresistivity.^[15] Although studies on exfoliated or deposited 2D flakes are promising, the lateral size of the samples is typically limited to the micrometer scale thus limiting their integration into real technological devices.

1. Introduction

Many of the foreseen active systems in near-future nanotechnology will be bendable and stretchable.^[1,2] This is required to meet the incipient demand for smart technologies able to adapt to arbitrary complex object shapes and combine everyday items


Conversely, the Xenex, the mono-elemental class among 2D materials, are typically deposited by epitaxial methods, thus ensuring large-scale uniformity.^[16] In this context, silicene is a promising candidate to scale up flexible devices on a cm² scale while holding the compatibility with a complementary metal oxide semiconductor platform, and more generally to the ubiquitous silicon semiconductor technology (even including flexible electronics). The silicene physical properties, however, are strongly affected by its most commonly used epitaxial template, that is, the (111)-terminated Ag surface, which, to some extent, can limit the range of technological exploitation of the 2D material. To overcome this limitation, we recently showed the silicene accommodation on an interfacial stanene layer introducing the scheme of the Xene heterostructures.^[17] On one hand, this configuration enables to tailor of the physical properties of the constituent layers by taking advantage of the proximity effect,^[18] and on the other hand, it expands the palette of potential technological exploitations of the Xenex, disclosing novel routes to material processing and to the heterogenous integration of dissimilar materials in functional technological platforms.^[19]

In this work, we introduce a process flow to experimentally fabricate cm² scale bendable silicene membranes starting from

C. Martella, C. Massetti, D. S. Dhungana, C. Grazianetti, A. Molle
CNR-IMM

Unit of Agrate Brianza
Agrate Brianza I-20864, Italy
E-mail: christian.martella@mdm.imm.cnr.it;
alessandro.molle@mdm.imm.cnr.it

C. Massetti, E. Bonera
Dipartimento di Scienza dei Materiali
Università degli Studi di Milano Bicocca
Via Cozzi-55, Milano I-20125, Italy

 The ORCID identification number(s) for the author(s) of this article can be found under <https://doi.org/10.1002/adma.202211419>

© 2023 The Authors. Advanced Materials published by Wiley-VCH GmbH. This is an open access article under the terms of the Creative Commons Attribution License, which permits use, distribution and reproduction in any medium, provided the original work is properly cited.

DOI: 10.1002/adma.202211419

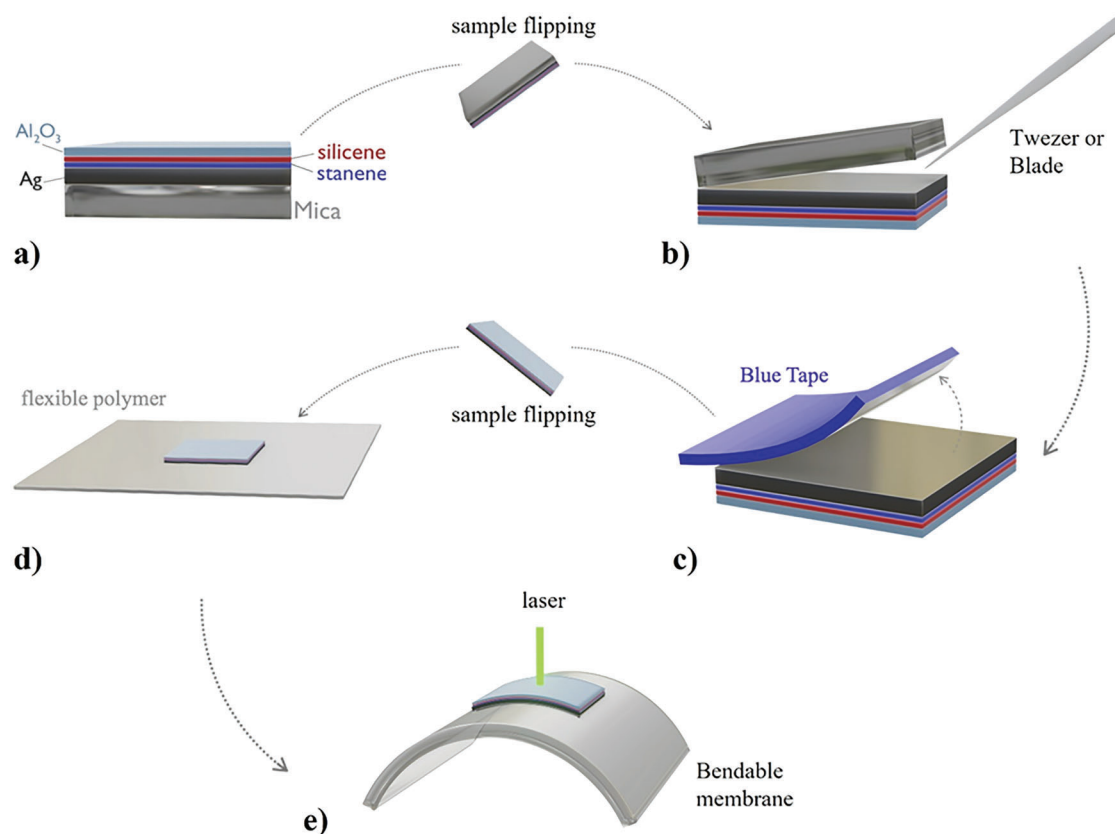


Figure 1. Schematics of the processing steps used for the fabrication of silicene-based membranes. a) After the deposition of silicene (or silicene–stanene heterostructure) and of the Al_2O_3 capping layer, the sample is flipped for mica mechanical delamination with b) tweezers and c) blue Nitto tape. d) The sample is then flipped back and attached to a new target flexible substrate allowing characterization of the properties of the bendable membranes under mechanical deformation (e). See Figure S7 (Supporting Information) containing the Raman spectra of the sample during the (a–e) process steps.

mono and multilayer silicene and silicene–stanene heterostructures epitaxially supported by Ag(111) substrates. Specifically, we use micro-Raman spectroscopy to monitor the strain applied to the bent silicene layer when embedded into different configurations, therein showing that the so-obtained membranes are strain-responsive up to 0.6% tensile deformation value. We experimentally deduce the spectral Raman shift per % of uniaxial strain to be as high as $-7.7 \text{ cm}^{-1} \text{ \%}^{-1}$ in the heterostructure configuration. In particular, the introduction of the stanene layer in the silicene–stanene heterostructure is effective in lowering the electronic interaction of silicene with Ag(111) but concomitantly favoring the transfer of the applied strain via the metal substrate.

2. Results and Discussion

The experimental details of the mono- and multilayer silicene and silicene–stanene epitaxy on Ag(111)/mica substrates are briefly summarized in Experimental Section and Supporting Information (see Figures S1–S6, Supporting Information), more details are reported in ref. [17] The fabrication steps of the bendable silicene membranes are summarized in **Figure 1a–e** and Figure S7 (Supporting Information). From top to bottom, the starting sample configuration includes an Al_2O_3 capping layer, active Xenes layers (silicene or silicene–stanene), and the

Ag(111)/mica substrate as a template. The special constitution of the epitaxial template allows for a complete disassembling of the silicene-based stack as previously described.^[20] The process starts by flipping back the whole stack and with the mechanical removal of a bulk part of the native mica substrate (Figure 1b). Then the delamination is further refined by means of multiple scotch-tape (3M blue Nitto tape) peelings, thus leaving only some residual layers of mica (Figure 1c). Subsequently, the sample can be turned upside down (as in Figure 1a but without mica layers) and attached to a secondary host substrate, namely a flexible polymer substrate, using a double-sided tape (Figure 1d,e). The polymer used here as carrier substrate is a commercial polyethylene terephthalate (PET) sheet that was preferably chosen for its good thermal and chemical stability.^[21] We stress that this transfer process is universally applicable to any other kind of flexible substrates like thin metal foils, amorphous (polycarbonate) or semi-crystalline thermoplastic polymers (polypropylene), bio-compatible and -resorbable materials (cellulose, collagen, silk fibroin, etc.), owing to the chemical and structural stability of the Xenes layers in the heterostructure no matter of the final destination of the transfer.^[1,22–25]

We use Raman spectroscopy as a probe to monitor the response of the samples against an applied mechanical deformation.^[26] Based on the Raman spectrum of monolayer

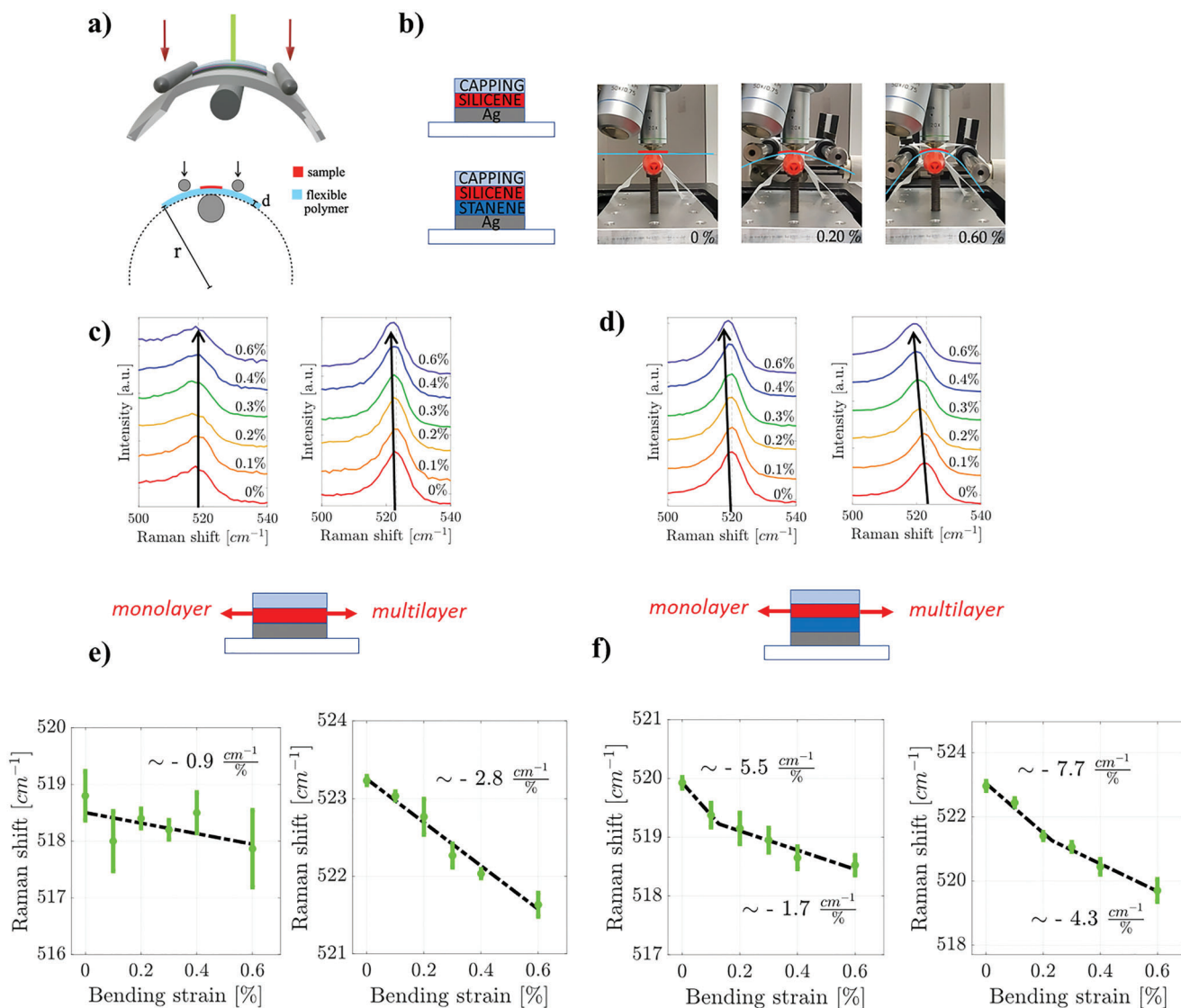


Figure 2. Raman spectroscopy strain-responsivity of the silicene membranes. a) Sketch of the setup used for the application of macroscopic uniaxial strain to the bendable silicene membranes. It is a three-point bending tool consisting of a fixed central cylinder and two cylinders that move synchronously in the vertical direction. b) The bending instrument is installed under the microscope of the Raman spectroscopy setup for strain-dependent measurements. Optical pictures of the sample upon application of 0%, 0.2%, and 0.6% uniaxial strain (the silicene membrane and the supporting flexible substrate are in red and cyan, respectively). Raman investigations of the bendable membranes based on mono- and multilayer silicene c) without and d) with the stanene layer to form the heterostructure as a function of the applied strain. d) Frequency position of the Raman modes of the bendable membranes based on mono and multilayer silicene e) without and f) with the stanene layer to form the heterostructure as a function of the applied strain.

silicene on Ag(111),^[27] we expect a main peak related to the E_{2g} vibrational mode of the hexagonal Si rings located at wavevectors 516–520 cm^{-1} depending on the specific silicene surface superstructures (when referred to the Ag lattice parameters), and minor components at lower wavevectors essentially related to intrinsic disorder (non-uniform buckling or distortion of the hexagonal ring), see also Supporting Information.^[28] In the multilayer case, the Raman spectrum exhibits a blueshift of the main peak compared to that of the monolayer and the appearance of low-frequency components due to the preserved mixed sp^2 - sp^3 orbital hybridization, see Supporting Information.^[29]

In both cases (mono and multilayer), a variation of the Raman shift as a function of the applied deformation can be related to an extrinsically induced strain in the silicene layer provided that the incident laser power was kept below 5 mW to avoid optothermal effects. To better quantify the Raman response of the silicene membranes under externally applied bending momentum, we built a three-point bending device, whose operating principle is shown in **Figure 2** and Figure S8 (Supporting Information). The instrument consists of two cylinders placed on the same plane, the synchronous vertical displacement of the cylinders results in a controlled bending of the flexible sample sustained, at the

central position, by a fixed third cylinder. This is a conventional approach to study strain engineering in 2D materials and so envisages their potential exploitation in straintronic devices.^[30] The applied strain can be derived by measuring the radius of curvature of the sample assuming that the thickness of the sample is negligible compared to those of the flexible polymer and tape (total thickness d). Moreover, since d is much smaller than the radius of curvature of the osculating circle r (Figure 2a,b) the bending strain can be approximated as $\epsilon = d/2r$, and the sample is under pure tensile loading.^[31,14] This bending device has been installed in the Raman spectroscopy setup aiming at monitoring the evolution of the silicene vibrational mode under progressive increment of the tensile strain (Figure 2c–f). When increasing the applied uniaxial strain, the vibrational frequency of the silicene Raman mode is expected to redshift as a result of the increase of the Si–Si bond length and the relative decrease of the atomic interaction. In Figure 2c, the evolution of the Raman spectra displays differences in the vibrational response of the silicene-based membranes under the application of a tensile strain. The shape profile of the Raman peak of silicene is known to be asymmetric and can be then fitted with two Lorentzian–Gaussian components.^[27,32] As shown in Figure 2c, the main component related to the Raman mode in the monolayer silicene on Ag shows an extremely weak sensitivity to the application of the tensile strain in the range 0–0.6% (Figure 2c left panel). Strain sensitivity increases in the case of multilayer silicene on Ag (Figure 2c right panel), and more notably, when the stanene layer is introduced to form the heterostructure (Figure 2d left panel for the monolayer silicene on stanene, and right panel for the multilayer silicene on stanene). Larger-scale statistical inspection reveals that the observed shift of the Raman mode does not depend on the sample position enlightened by the laser spot, as one can infer from the mean value and standard deviation of the frequency position at different strain levels, see Figure 2. Quantitatively, performing a linear regression on the experimental data (see Table S1, Supporting Information for details), we notice that the mono and multilayer silicene membranes display a spectral shift rate of $-0.9 \text{ cm}^{-1} \%^{-1}$ and $-2.8 \text{ cm}^{-1} \%^{-1}$ respectively, while the corresponding heterostructures show more pronounced spectral shifts, see Figure 2e. In detail, the response of the heterostructures is more intriguing as it shows a bimodal regime, indeed the monolayer silicene on stanene presents a spectral shift rate of $-5.5 \text{ cm}^{-1} \%^{-1}$ up to 0.1% of uniaxial strain and $-1.7 \text{ cm}^{-1} \%^{-1}$ for larger strain value, see Figure 2f. The case of the multilayer silicene heterostructure shows spectral shift rates as high as $-7.7 \text{ cm}^{-1} \%^{-1}$ up to 0.2% of uniaxial strain and $-4.3 \text{ cm}^{-1} \%^{-1}$ for larger strain values.

In analogy with the model developed for graphene,^[26] we can use the strain-dependent Raman measurements shown in Figure 2e,f to derive the Grüneisen parameter, γ , for the silicene vibrational mode. Under uniaxial strain, the following equation links the strain-dependent peak position, $\omega(\epsilon)$, to γ :^[26]

$$\omega(\epsilon) - \omega_0 = -\omega_0 \gamma (1 - \nu) \epsilon \quad (1)$$

where ω_0 is the peak position at zero strain and ν is the Poisson's coefficient. Considering that no evidence of silicene delamination has been observed during the bending cycles and that, in all the considered samples, the Raman peak position after the ap-

plication of strain recovers its initial value, we can use in Equation (1) the Poisson coefficient of the thin Ag substrate ($\approx 300 \text{ nm}$), $\nu_{\text{Ag}} = 1/3$, see ref. [33] (we note that the chosen value is comparable also to the Poisson coefficient of the polymeric PET substrate, see ref. [26]). Combining Equation (1) with the data in Figure 2, we obtain for the monolayer and multilayer silicene: $\gamma_{\text{mono, Si}} = 0.26$ and $\gamma_{\text{multi, Si}} = 0.8$, respectively; while for the heterostructure case, we derive for the monolayer and multilayer silicene $\gamma_{\text{monoH, Si}} = 0.67$ and $\gamma_{\text{multiH, Si}} = 1.5$, respectively. To derive a single Grüneisen parameter for the heterostructures, we use the single component fit of the strain-dependent Raman response reported in Figure S4 (Supporting Information) (the parameters calculated considering the bimodal regime are reported in Supporting Information). We emphasize that theoretical studies on the vibrational properties of Xenes have predicted a strong dependence of the Grüneisen parameters on different configurational details, that is, buckling, applied strain (type, amount, etc.), and substrate interaction.^[34] As a result, even if a direct match with theoretically predicted values for unsupported silicene would not be grounded, our experimental data can be considered as the first quantitative estimation of the Grüneisen parameters for silicene in the specific configuration here considered.

In addition, we stress that all the tested samples have proven high repeatability of the strain-responsive behavior, along with robustness against mechanical fractures over more than one hundred bending cycles showing a reversible shift of the Raman peak frequency within the experimental uncertainty, see Figures S9, S10 (Supporting Information).

The comparative study of the silicene membranes, that is, with and without the stanene layer, leads us to conclude that the mechanical and electronic properties of silicene are decisively affected by the interaction with the substrate in a different way.^[35] On the one hand, the dependence of the silicene electronic properties on the Ag(111) is dramatically reduced when the stanene buffer layer is placed in between, being consistent with the recently reported optothermal properties of silicene–stanene heterostructures in response to laser-induced local heating.^[32] On the other hand, the structural models of the silicene–stanene heterostructures, carried out in a density functional theory framework,^[17] have demonstrated a geometrical intermixing of the Xene layers which is responsible for the observed improved strain transfer when stanene is incorporated in the membrane.

The adopted bending instrument allowed us to test the strain-responsivity of the membranes on a macroscopic (\approx millimeters) length scale of mechanical deformation. Nevertheless, it is also interesting to test the strain responsivity on a length scale compatible with the micro- or nano-scale of typical device architectures. In this respect, wrinkle formation has been reported as an effective strategy to localize a large level of stress into a limited (from a few microns to hundreds of nanometres scale, typically) spatial portion of 2D materials, thus allowing for strain-engineering of the material's properties.^[11] In our approach, we intentionally induced micro-scale uniaxial wrinkle formation into the more strain-responsive membrane, namely the multilayer silicene–stanene heterostructure, by releasing a certain amount of elastic tension during the detachment of the membranes from the flexible polymer substrate (see sketch and optical microscope image in Figure 3). To quantitatively describe

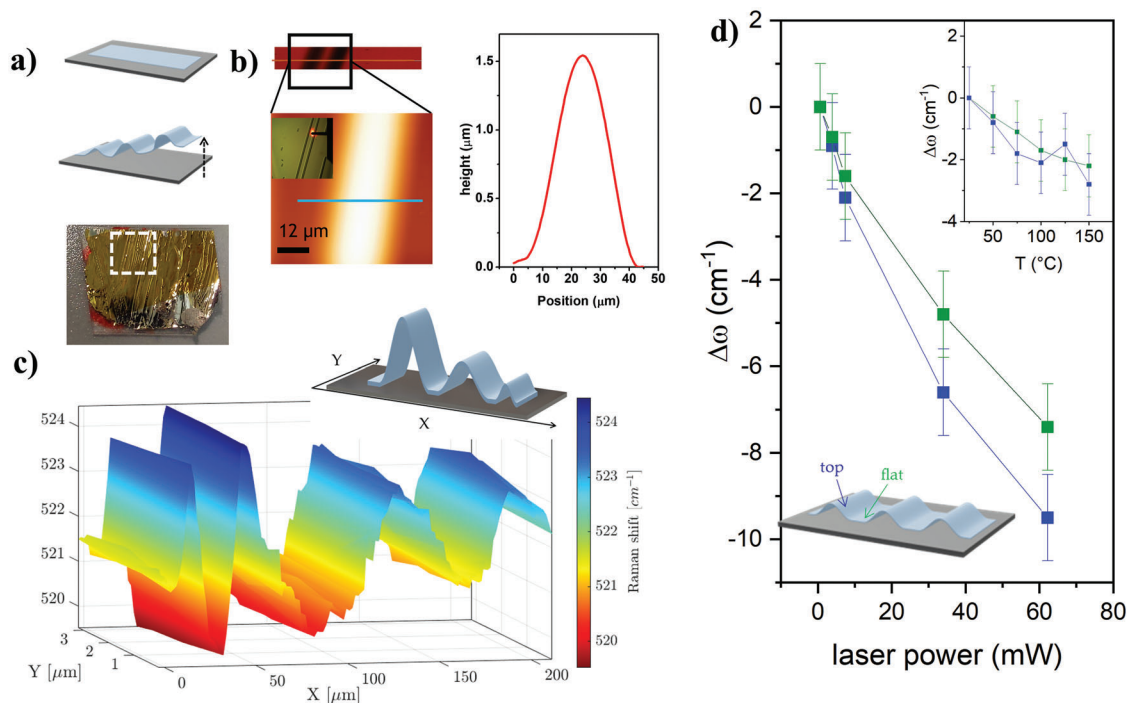


Figure 3. Micro-strain deformation to set in wrinkles in silicene membranes. a) Cartoon of the tension release process that leads to the formation of micro-wrinkles into the membranes and an optical picture of a sample with the indication of the wrinkled area. b) AFM topography and height profile of a selected wrinkle. c) Spatial map of the frequency position of the main silicene Raman peak. Inset: a sketch of the wrinkles mapped in the Raman measurements. d) Opto-thermal measurements of the Raman modes at the strained (top) and unstrained (flat) region of the wrinkled membrane. The measurements are carried out by varying the incident laser power in the range of 0.5–60 mW. Inset: thermal measurements obtained by globally heating the sample on a hot plate in the range of 25–150 °C.

the morphological and strain distribution throughout the wrinkles, we compare atomic force microscopy (AFM) with Raman spectroscopy mapping across the wrinkle modulation. According to the topography and height profile of Figure 3b, a single wrinkle has a mean lateral size $L \approx 35 \mu\text{m}$, and vertical displacement $H \approx 1.5 \mu\text{m}$. The maximum of the uniaxial tensile strain, ϵ , is accumulated at the top of the wrinkle and can be estimated according to the conventional strain model for 2D materials:^[11]

$$\epsilon = \frac{\pi^2 h d}{(1 - \nu^2) l^2} \quad (2)$$

Where d is the thickness of the wrinkled sample, h and l are respectively the vertical displacement and the lateral size of the wrinkle where the profile can be approximated to a circular shape (we considered $h \approx 0.5 \mu\text{m}$ from the topmost of the wrinkle in Figure 3b corresponding to $l \approx 15 \mu\text{m}$), and ν is the Poisson's coefficient of the wrinkled material. We note that wrinkles with similar morphological features have been observed in the reference sample made by only the Ag/Al₂O₃ stack, see AFM investigations in Figure S11 (Supporting Information). This fact suggests that the silicene/stanene wrinkles conformally replicate the surface modulations produced in the metallic substrate without delamination from it. As a result, to a first approximation, we can substitute in Equation (2) the Poisson's coefficient of a thin Ag film ($d \approx 300 \text{ nm}$), $\nu_{\text{Ag}} = 1/3$.^[33] With these values, Equation (2) pro-

vides a percent tensile strain at the top of the wrinkle of $\approx 0.7\%$. Considering that Young's modulus of the stack can be approximated with that of the thin Ag film, $E_{\text{Ag}} = 80 \text{ GPa}$,^[36] and applying Hooke's law ($\sigma = \epsilon E$), the maximum stress in the wrinkles turns out to be 250 MPa. Figure 3c shows the map of the Raman peak shift induced by the local curvature of the wrinkles. From the analysis of the Raman map, we inferred that the Raman peak frequency undergoes strong variation as a function of the spatial position. In particular, large frequency shifts are observed between the flat region (peak position $\approx 523\text{--}524 \text{ cm}^{-1}$, in agreement with the data at zero strain value in Figure 2d) and the crest of the wrinkles, where the Raman peak positions shift toward lower wavevectors as a function of the wrinkled morphology (lateral size and height amplitude).

We should note that the maximum frequency shift ($\approx -3 \text{ cm}^{-1}$) is measured on top of the wrinkle investigated by AFM with respect to the flat region. By matching this value with the results of the mechanical deformation applied on the macroscale (Figure 2d), we expect a strain of $\approx 0.6\%$ in good agreement with the value derived using Equation (2).

Notably, the wrinkled geometry allowed us to easily access a strain-dependent trend of the thermal response of the silicene–stanene membrane heterostructures. This is performed by combining thermal Raman measurements, obtained by globally heating the sample with a hotplate, with optothermal Raman spectroscopy, in which the laser source is not only used as a detection probe but also as a local heater with a released thermal energy

dependent on the incident light power.^[32] The temperature dependence of Raman peak positions can be described by the linear relation $\Delta\omega = \omega(T) - \omega_0 = \chi_T T$,^[37] where $\omega(T)$ and ω_0 are the peak position at temperature T and room temperature, respectively, and χ_T is the temperature coefficient. In the inset of Figure 3d, we notice that, in the flat region (green symbols), the Raman peak position clearly displays a decreasing trend when the temperature increases. Linear regression to the data allows us to quantitatively assess the temperature coefficient of the flat region $\chi_{T,\text{flat}} \approx -0.018 \pm 0.002 \text{ cm}^{-1} \text{ }^\circ\text{C}^{-1}$. By a closer insight into the data, one can notice that, for the considered temperature range, the thermal Raman response does not show significant differences considering the flat and top regions of the wrinkles. Quantitatively, the temperature coefficient at the top of the wrinkles is $\chi_{T,\text{top}} \approx -0.019 \pm 0.005 \text{ cm}^{-1} \text{ }^\circ\text{C}^{-1}$, that is within the data uncertainty of the measurements on the flat region. It is instructive to make a comparative study of the Raman responses as a function of the temperature rise induced by the two presented methodologies (i.e., hotplate and laser power respectively). As expected, the larger Raman shift observed in the optothermal measurements indicates that the temperature induced by the laser heating at the highest power is far higher than 150 °C.

In analogy with the hotplate measurements, the power dependence of the Raman peak positions can be described by the linear relation $\Delta\omega = \omega(P) - \omega_0 = \chi_p P$,^[32] where $\omega(P)$ and ω_0 are the peak position at power P and P_{min} = minimum laser power, respectively, and χ_p is the power coefficient. A linear regression of the data allows us to quantitatively assess the power coefficient of the flat region, $\chi_{p,\text{flat}} \approx -0.11 \pm 0.01 \text{ cm}^{-1} \text{ mW}^{-1}$, and top region $\chi_{p,\text{top}} \approx -0.15 \pm 0.01 \text{ cm}^{-1} \text{ mW}^{-1}$. Due to the local nature of the laser-induced heating mechanism (laser spot size $\approx 1 \mu\text{m}$), the optothermal measurements involve a response to a temperature gradient in the sample, which points to a different thermal conduction in strain (flat) and unstrained (top) domains.

Moreover, we stress that the derived power and thermal coefficients should be considered as experimental parameters of the combined silicene/stanene/Ag stack, since the substrate plays a role in the heat dissipation in both the thermal and opto-thermal configurations.

Despite theoretical calculations that consider the level of stress sensibly higher than the one derived at the top of the wrinkles, an unusual strain dependence of the thermal conductivity in silicene is predicted to be mainly due to the change (enhancement) in acoustic phonon lifetime.^[38] As a matter of fact, such an enhancement plausibly originates from the flattening of the buckled silicene structure upon stretching or other related structural modification of the silicene structure during the wrinkling procedure.^[38]

Finally, we show how the bendable silicene membranes discussed so far can be introduced into a technology-oriented process flow. To this scope, we explored two different approaches for nano- and micro-fabrication of metal pads in electrical contact with the silicene layers. First, we demonstrate that a device pattern on the silicene samples can be defined both at the beginning (Figure 1a) and at the end (Figure 1d) of the process flow described in Figure 1. In the former case, a device pattern is defined before the mica delamination and then transferred on a substrate, see Experimental Section and Figure 4a–c. This way we generally show that the device can be supported and inte-

grated into any arbitrary rigid or flexible substrate after transfer of the pre-patterned samples. For example, in Figure 4c the devices are supported by both the PET polymer (left) and a commercial paper sheet (right). In the latter case, we note that the PET substrate exhibits good thermal and solvent resistance, therefore, the nano- and micro-fabrication of metal electrical contacts on the membranes can be easily achieved by means of photolithographic steps directly on the flexible substrate after mica delamination (see Figure S12, Supporting Information). To evaluate the degree of bendability of the device, the membranes endowed with patterned electrodes are wrapped around commonly used lab objects having a circular section with a diameter in the range of 9–60 mm (see Figure 4; Figures S13, S14, Supporting Information). Note that the corresponding applied strain is also reported for each radius of curvature, and that the variation of the Raman peak position for the wrapped membranes (see Figure S14, Supporting Information) is in good agreement with the bending tests obtained by using the three-point terminal described above and reported in Figure 2. All the silicene-based membranes remain so-wrapped for days without visible structural damage. This is confirmed by the Raman analysis, which shows the almost negligible variation of the mode intensity and spectral position over the entire temporal window and after the detachment from the objects, see Figure 4e.

The second approach for the definition of the electrical contacts on the multilayer silicene–stanene heterostructure combines the methodology presented here with the “silicene encapsulated delamination with native electrodes” (SEDNE) process that we previously developed for the silicene samples.^[20,39] In detail, after the complete mica delamination obtained in Figure 1c, the sample is attached on the flexible substrate without flipping it, in this way the silver substrate is exposed and can be used for the microfabrication of the electrical contacts, see Experimental Section and sketch in Figure 4f. The so-obtained two-terminal passive device can be tested as a prototypical piezoresistor, where the electrical resistance is measured as a function of the applied strain (see the used setup in Figure S15 in Supporting Information). In Figure 4f, a sizeable variation (increment) of the electrical resistance is real-time observed by applying three different strain values (0.4%, 0.5%, and 0.6%) to the sample in a sequence of bending cycles. Note that the initial value at zero strain, R_0 ($\approx 1.1 \text{ M}\Omega$), is recovered after each bending cycle thus demonstrating the repeatability of the piezo-resistive effect and durability of the sample.

3. Conclusion

In conclusion, we have demonstrated that bendable silicene-based membranes can be obtained starting from epitaxial mono and multilayer silicene grown on Ag(111) or in a heterostructure configuration, where a stanene layer decreases the electronic interaction of silicene with the metal substrate and enhances the mechanical transfer of the applied strain as demonstrated by the largest Raman shift observed. These configurations enabled us to investigate the silicene response to the strain on both the macro and micro scale by means of Raman spectroscopy. In particular, in the case of the silicene–stanene heterostructures, the largest responsivity to strain has been disclosed for the multilayer silicene, thus making it promising for applications in flexible

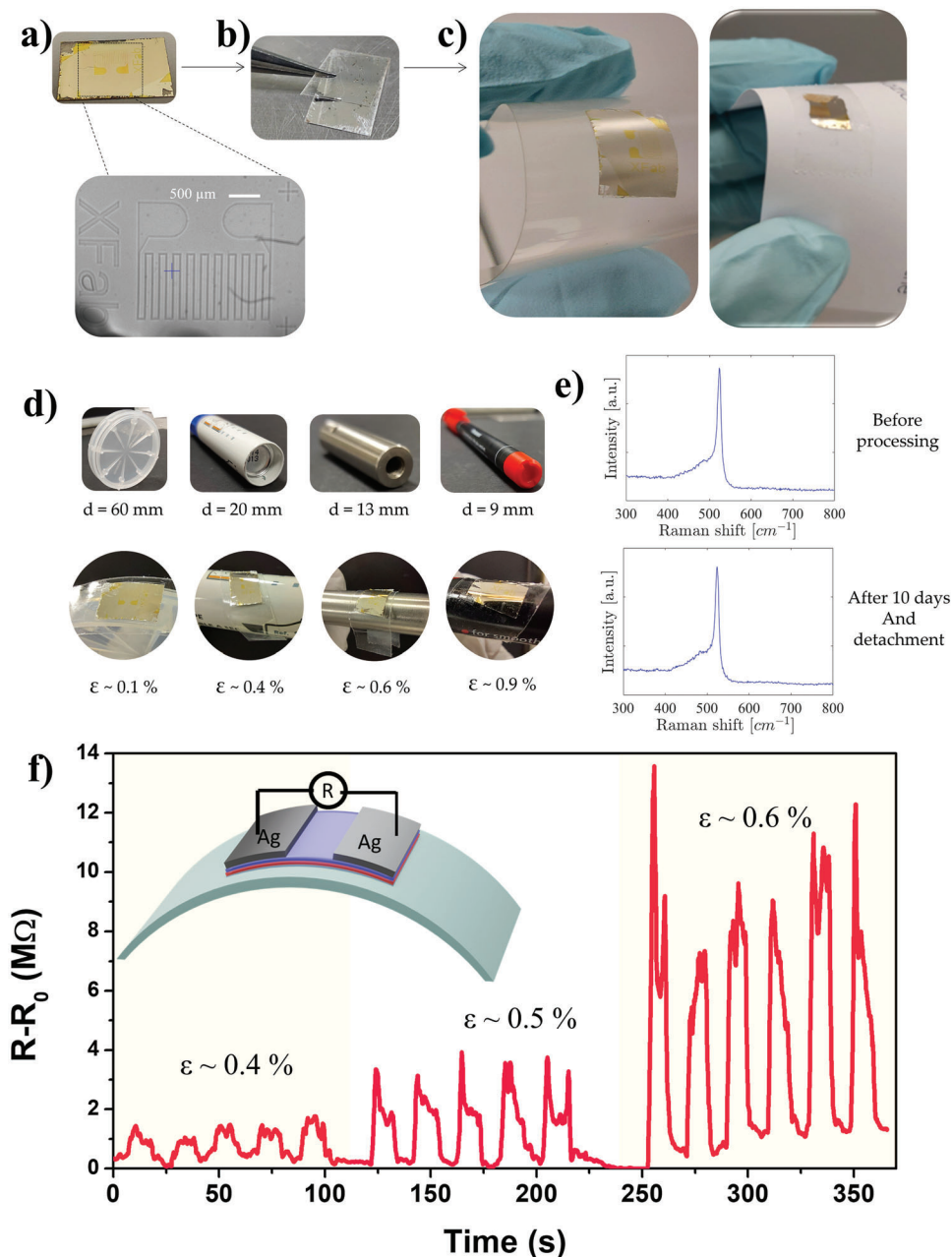


Figure 4. Processing and electrical characterization of device patterns defined onto the membranes. a) After the Xenes and Al_2O_3 deposition, the sample is taken out of the vacuum and subsequently patterned by means of optical lithography, thus obtaining the electrical contacts after the metal deposition and subsequent liftoff, as for example, a microheater or the XFab logo. b) The sample is flipped for mica delamination through tweezers, and then c) it is flipped again to be attached to an arbitrary flexible/rigid substrate (a PET polymer or a paper sheet in the photo). d) Images of the common lab objects used to wrap the membranes. Each object has a different diameter d associated with a different strain value ϵ . e) Raman characterization of the membrane before the processing and after ten days of being wrapped. f) Measurements of the electrical resistance of a two-terminal passive device obtained by a combination of the methodologies described in Figure 1 and the SEDNE approach developed for the silicene samples in refs. [20,39].

electronics. The so-proposed process flow can be generally extended to the class of the epitaxial Xenes, and readily applicable to Ag-supported Xenes like borophene, antimonene, and stanene.^[40–43] In particular, for the silicene case, our findings pave the way to introduce dimensionally reduced silicon, both in the stand-alone or heterostructure configurations, into flexible and strain-responsive applications.

4. Experimental Section

Xenes Growth: Silicene and stanene layers were grown using the Scienta Omicron LAB10 MBE system which was equipped with Low Energy Electron Diffraction and Auger Electron Spectroscopy probes for in situ characterization. As mentioned elsewhere in detail,^[17] a typical sample production scheme followed three steps: preparation, growth, and encapsulation. Several cycles of sputtering and subsequent annealing ($\approx 550^\circ\text{C}$)

were performed on commercial Ag(111)/mica substrates before Xenex growth. The deposition was carried out by means of molecular beam epitaxy in an ultra-high vacuum chamber system at a base pressure of 10^{-10} mbar keeping the substrate at 200–225 °C. For heterostructures, first a Sn layer was deposited on the prepared substrate, then the Si layer was deposited on top of Sn. The multilayer silicene (3 MLs) samples were obtained by increasing the deposition time of Si evaporation that was pre-calibrated by means of a quartz microbalance. The same multilayer silicene thickness was considered in the two configurations discussed (i.e., with and without stanene) for a fair comparison. After the growth, the Xenex samples were protected against oxidation by encapsulation, namely the in situ sequential deposition of a 5 nm thick Al_2O_3 capping layer by means of reactive molecular beam deposition.^[44]

Characterizations: Raman measurements were performed using a Renishaw InVia spectrometer in a backscattering configuration with a continuous-wave 514 nm excitation coupled to a Leica optical microscope equipped with a 50× (0.75 numerical aperture) objective. The diffraction grating in use was constituted by 2400 grooves mm^{-1} with a corresponding spectral resolution of 1–2 cm^{-1} . In order to test the Raman response of the silicene membranes, the laser power was kept below 5 mW and all the spectra were acquired collecting 3 accumulations with an exposure time of 10 s. In the case of optothermal measurements, the laser power was varied between 0.5 and 60 mW by acquiring each spectrum collecting 3 accumulations with an exposure time of 20 seconds. Thermal Raman measurements were performed by using a reasonably low laser power (1 mW) varying the temperature of the sample in the range of 25–150 °C. The temperature variation was applied by accommodating the samples on a resistive hotplate. The upper limit represented the maximum temperature value at which the PET substrate showed structural stability. As a matter of fact, by further increasing the temperature, the appearance of random plastic deformation of the substrate was noticed.

The AFM investigation of the samples was performed in tapping mode with an AFM-Bruker commercial system (Dimension Edge) equipped with ultra-sharpened silicon tips (Bruker TESP V-2, nominal tip radius 7–10 nm).

Photolithography and Electrical Characterization: The samples patterned at the beginning (Figure 1a) and at the end (Figure 1d) of the process flow described in Figure 1 were processed as follows. The electrical contacts were made by defining the pattern through optical lithography using the Tabletop Maskless Aligner μMLA from Heidelberg followed by the etching of the protective (5 nm thick) Al_2O_3 capping layer. The Al_2O_3 layer was etched by immersing, for ≈ 1 min, the sample in hydrofluoric acid (HF) diluted in de-ionized water at a volume ratio of 1:50. After removing the alumina, a deposition of 5 nm of Ti followed by 50 nm of Au was carried out using the evaporation system Auto 304 from Edwards and finally, the lift-off was performed. The samples patterned after the complete mica delamination obtained in Figure 1c were processed using the SEDNE methodology. Specifically, the mica layer was first removed mechanically and then the sample was attached to a target substrate (PET) with the Ag layer facing upward. The silicene channel and the electrodes in the native Ag layer were patterned through optical lithography using the Tabletop Maskless Aligner μMLA by Heidelberg followed by Ag etching realized by immersing the sample in a homemade aqueous solution consisting of potassium iodide (KI) and iodine (I_2). The electrical resistance measurements were carried out by means of a Keithley Model 2000 Multimeter controlled by using LabVIEW software.

Statistical Analysis: Each Raman spectrum acquired was fitted with a two-component curve, using the Voigt profiles, through the WiRE (Windows-based Raman Environment) software by Renishaw, in order to extrapolate the peak position values. For each type of sample and for every applied strain value, the Raman spectrum was acquired in ten different spatial positions of the sample surface within an area of $\approx 100 \mu\text{m}^2$. In this way, it was possible to express the peak position value as mean \pm standard deviation (SD). The points obtained with the respective error bars were then linearly fitted, through MATLAB software, evaluating the goodness-of-fit statistics through the Chi-Square method.

To obtain the approximate strain values to which each sample was subjected, photos from the same position and angle were taken of the curved PET substrate and analyzed using vector graphics software. Specifically,

the authors calculated the maximum and minimum diameter of the circumferences that best approximated the curvature and used the average value to extrapolate the strain value (the thickness of the PET was known).

Supporting Information

Supporting Information is available from the Wiley Online Library or from the author.

Acknowledgements

Mario Alia and Simone Cocco (both at CNR-IMM) are acknowledged for technical support. This research was funded by European Commission within the H2020 research and innovation program under the ERC-COG 2017 grant no. 772261 “XFab” and ERC-PoC 2022 Grant N. 101069262 “XMem”.

Author Contributions

Chr.M., C.G., and A.M. conceived, designed, and coordinated the experiments. D.S.D. performed epitaxial growth of Xenex with in situ characterization. C.M. delaminated the Xenex membranes, performed the bending experiments, and lithographically patterned the membranes. Chr.M., E.B., and C.M. carried out Raman spectroscopy studies. Chr.M. performed AFM studies. Chr.M. and C.M. performed the electrical characterization of the prototypical devices. A.M. coordinated and supervised the research, provided, and managed the technical resources. All authors contributed to the writing based on the draft written by Chr.M. All authors have given approval to the final version of the manuscript.

Conflict of Interest

The authors declare no conflict of interest.

Data Availability Statement

The data that support the findings of this study are available from the corresponding author upon reasonable request.

Keywords

2D, membranes, piezoresistivity, silicene, strain engineering, Xenex heterostructures

Received: December 6, 2022
Revised: April 28, 2023
Published online: June 26, 2023

- [1] S. Gupta, W. T. Navaraj, L. Lorenzelli, R. Dahiya, *npj Flexible Electron.* **2018**, *2*, 8.
- [2] D. Akinwande, N. Petrone, J. Hone, *Nat. Commun.* **2014**, *5*, 5678.
- [3] A. Daus, S. Vaziri, V. Chen, Ç. Köroğlu, R. W. Grady, C. S. Bailey, H. R. Lee, K. Schauble, K. Brenner, E. Pop, *Nat. Electron.* **2021**, *4*, 495.
- [4] L. T. Quynh, C.-W. Cheng, C.-T. Huang, S. S. Raja, R. Mishra, M.-J. Yu, Y.-J. Lu, S. Gwo, *ACS Nano* **2022**, *16*, 5975.
- [5] X. Han, K. J. Seo, Y. Qiang, Z. Li, S. Vinnikova, Y. Zhong, X. Zhao, P. Hao, S. Wang, H. Fang, *npj Flexible Electron.* **2019**, *3*, 9.

- [6] C. Di Giorgio, E. Blundo, G. Pettinari, M. Felici, F. Bobba, A. Polimeni, *Adv. Mater. Interfaces* **2022**, *9*, 2102220.
- [7] L. Gao, *Small* **2017**, *13*, 1603994.
- [8] H. Peelaers, C. G. Van de Walle, *Phys. Rev. B* **2012**, *86*, 241401.
- [9] F. Carrascoso, H. Li, R. Frisenda, A. Castellanos-Gomez, *Nano Res.* **2021**, *14*, 1698.
- [10] I. Niehues, R. Schmidt, M. Drüppel, P. Marauhn, D. Christiansen, M. Selig, G. Berghäuser, D. Wigger, R. Schneider, L. Braasch, R. Koch, A. Castellanos-Gomez, T. Kuhn, A. Knorr, E. Malic, M. Rohlfing, S. Michaelis de Vasconcellos, R. Bratschitsch, *Nano Lett.* **2018**, *18*, 1751.
- [11] A. Castellanos-Gomez, R. Roldán, E. Cappelluti, M. Buscema, F. Guinea, H. S. J. van der Zant, G. A. Steele, *Nano Lett.* **2013**, *13*, 5361.
- [12] T. Sohler, D. Campi, N. Marzari, M. Gibertini, *Phys. Rev. Mater.* **2018**, *2*, 114010.
- [13] T. Liu, S. Liu, K.-H. Tu, H. Schmidt, L. Chu, D. Xiang, J. Martin, G. Eda, C. A. Ross, S. Garaj, *Nat. Nanotechnol.* **2019**, *14*, 223.
- [14] I. M. Datye, A. Daus, R. W. Grady, K. Brenner, S. Vaziri, E. Pop, *Nano Lett.* **2022**, *22*, 8052.
- [15] F. Li, T. Shen, C. Wang, Y. Zhang, J. Qi, H. Zhang, *Nano-Micro Lett.* **2020**, *12*, 106.
- [16] C. Grazianetti, C. Martella, A. Molle, *Phys. Status Solidi RRL* **2020**, *14*, 1900439.
- [17] D. S. Dhungana, C. Grazianetti, C. Martella, S. Achilli, G. Fratesi, A. Molle, *Adv. Funct. Mater.* **2021**, *31*, 2102797.
- [18] J. F. Sierra, J. Fabian, R. K. Kawakami, S. Roche, S. O. Valenzuela, *Nat. Nanotechnol.* **2021**, *16*, 856.
- [19] H. Kim, S. Lee, J. Shin, M. Zhu, M. Akl, K. Lu, N. M. Han, Y. Baek, C. S. Chang, J. M. Suh, K. S. Kim, B. I. Park, Y. Zhang, C. Choi, H. Shin, H. Yu, Y. Meng, S. Il Kim, S. Seo, K. Lee, H. S. Kum, J. H. Lee, J. H. Ahn, S. H. Bae, J. Hwang, Y. Shi, J. Kim, *Nat. Nanotechnol.* **2022**, *2022*, 1.
- [20] C. Martella, G. Faraone, M. H. Alam, D. Taneja, L. Tao, G. Scavia, E. Bonera, C. Grazianetti, D. Akinwande, A. Molle, *Adv. Funct. Mater.* **2020**, *30*, 2004546.
- [21] W. A. MacDonald, M. K. Looney, D. MacKerron, R. Eveson, R. Adam, K. Hashimoto, K. Rakos, *J. Soc. Inf. Disp.* **2007**, *15*, 1075.
- [22] B. Zhu, H. Wang, W. R. Leow, Y. Cai, X. J. Loh, M.-Y. Han, X. Chen, *Adv. Mater.* **2016**, *28*, 4250.
- [23] J. Kim, A. Banks, H. Cheng, Z. Xie, S. Xu, K.-I. Jang, J. W. Lee, Z. Liu, P. Gutruf, X. Huang, P. Wei, F. Liu, K. Li, M. Dalal, R. Ghaffari, X. Feng, Y. Huang, S. Gupta, U. Paik, J. A. Rogers, *Small* **2015**, *11*, 906.
- [24] R. S. Dahiya, S. Gennaro, *IEEE Sens. J.* **2013**, *13*, 4030.
- [25] D. Zhao, Y. Zhu, W. Cheng, W. Chen, Y. Wu, H. Yu, *Adv. Mater.* **2021**, *33*, 2000619.
- [26] T. M. G. Mohiuddin, A. Lombardo, R. R. Nair, A. Bonetti, G. Savini, R. Jalil, N. Bonini, D. M. Basko, C. Galiotis, N. Marzari, K. S. Novoselov, A. K. Geim, A. C. Ferrari, *Phys. Rev. B* **2009**, *79*, 205433.
- [27] E. Cinquanta, E. Scalise, D. Chiappe, C. Grazianetti, B. van den Broek, M. Houssa, M. Fanciulli, A. Molle, *J. Phys. Chem. C* **2013**, *117*, 16719.
- [28] E. Scalise, E. Cinquanta, M. Houssa, B. van den Broek, D. Chiappe, C. Grazianetti, G. Pourtois, B. Ealet, A. Molle, M. Fanciulli, V. V. Afanas'ev, A. Stesmans, *Appl. Surf. Sci.* **2014**, *291*, 113.
- [29] C. Grazianetti, E. Cinquanta, L. Tao, P. De Padova, C. Quaresima, C. Ottaviani, D. Akinwande, A. Molle, *ACS Nano* **2017**, *11*, 3376.
- [30] O. Çakıroğlu, J. O. Island, Y. Xie, R. Frisenda, A. Castellanos-Gomez, *Adv. Mater. Technol.* **2022**, *8*, 2201091.
- [31] R. Schmidt, I. Niehues, R. Schneider, M. Drüppel, T. Deilmann, M. Rohlfing, S. M. de Vasconcellos, A. Castellanos-Gomez, R. Bratschitsch, *2D Mater.* **2016**, *3*, 021011.
- [32] E. Bonaventura, D. S. Dhungana, C. Martella, C. Grazianetti, S. Macis, S. Lupi, E. Bonera, A. Molle, *Nanoscale Horiz.* **2022**, *7*, 924.
- [33] G. N. Greaves, A. L. Greer, R. S. Lakes, T. Rouxel, *Nat. Mater.* **2011**, *10*, 823.
- [34] X.-J. Ge, K.-L. Yao, J.-T. Lü, *Phys. Rev. B* **2016**, *94*, 165433.
- [35] E. Cinquanta, G. Fratesi, S. dal Conte, C. Grazianetti, F. Scotognella, S. Stagira, C. Vozzi, G. Onida, A. Molle, *Phys. Rev. B* **2015**, *92*, 165427.
- [36] H. Mizubayashi, J. Matsuno, H. Tanimoto, *Scr. Mater.* **1999**, *41*, 443.
- [37] T. Wang, R. Wang, P. Yuan, S. Xu, J. Liu, X. Wang, *Adv. Mater. Interfaces* **2017**, *4*, 1700233.
- [38] H. Xie, T. Ouyang, É. Germaneau, G. Qin, M. Hu, H. Bao, *Phys. Rev. B* **2016**, *93*, 075404.
- [39] L. Tao, E. Cinquanta, D. Chiappe, C. Grazianetti, M. Fanciulli, M. Dubey, A. Molle, D. Akinwande, *Nat. Nanotechnol.* **2015**, *10*, 227.
- [40] Y. Shao, Z.-L. Liu, C. Cheng, X. Wu, H. Liu, C. Liu, J.-O. Wang, S.-Y. Zhu, Y.-Q. Wang, D.-X. Shi, K. Ibrahim, J.-T. Sun, Y.-L. Wang, H.-J. Gao, *Nano Lett.* **2018**, *18*, 2133.
- [41] B. Feng, J. Zhang, Q. Zhong, W. Li, S. Li, H. Li, P. Cheng, S. Meng, L. Chen, K. Wu, *Nat. Chem.* **2016**, *8*, 563.
- [42] J. Yuhara, Y. Fujii, K. Nishino, N. Isobe, M. Nakatake, L. Xian, A. Rubio, G. Le Lay, *2D Mater.* **2018**, *5*, 025002.
- [43] S. Sun, J. Y. You, S. Duan, J. Gou, Y. Z. Luo, W. Lin, X. Lian, T. Jin, J. Liu, Y. Huang, Y. Wang, A. T. S. Wee, Y. P. Feng, L. Shen, J. L. Zhang, J. Chen, W. Chen, *ACS Nano* **2022**, *16*, 1436.
- [44] A. Molle, G. Faraone, A. Lamperti, D. Chiappe, E. Cinquanta, C. Martella, E. Bonera, E. Scalise, C. Grazianetti, *Faraday Discuss.* **2020**, *227*, 171.